Mechanics of Materials 70 (2014) 41–52

Contents lists available at ScienceDirect

Mechanics of Materials

journal homepage: www.elsevier.com/locate/mechmat

Impact of thick PMMA plates by long projectiles at low velocities. Part I: Effect of head's shape

D. Rittel *, A. Dorogoy

Faculty of Mechanical Engineering, Technion – Israel Institute of Technology, 32000 Haifa, Israel

ARTICLE INFO

Article history:
Received 30 June 2013
Received in revised form 16 October 2013
Available online 11 December 2013

Keywords:
Penetration
Resisting force
Finite elements
Impact
Long projectiles
PMMA

ABSTRACT

A hybrid experimental–numerical investigation of the penetration process in thick polymethylmethacrylate (PMMA) plates was carried out. The response of such plates to the impact of long hard steel projectiles having either blunt, hemispherical or ogive-head shapes was investigated experimentally in the range of velocities of 100 (m/s) < V_0 < 250 (m/s). The penetration process can be divided into 3 stages: entrance, propagation and backwards bouncing. The last two stages are associated with brittle fracture of the plates. The tests were modeled using 3D explicit finite element analyses. The numerical results provide insight regarding the variations of field variables such as stresses, velocities, resisting forces and energies. A good agreement regarding the trajectory of the projectile and the depths of penetration is obtained. The enhanced backwards bouncing phenomenon is explained, and it is shown that the average deceleration during the penetration process is constant. The resisting force to the penetration is higher for blunt projectiles. It is 10% lower for the hemispherical head and 50% lower for ogive-headed projectiles.

1. Introduction

Glassy polymers such as polymethylmethacrylate (PMMA) are an appealing choice for armor related applications due to their material properties such as pressure sensitivity, strain rate dependent strength, low density, transparency, dimensional stability and high durability. For this purpose, it is essential to have a comprehensive understanding of their dynamic behavior. Satapathy and Bless (2000) showed that during punch experiments, PMMA fractures in a brittle fashion in the absence of external confinement. The application of a sufficient external confinement causes its constitutive response to become elastic–plastic. The mechanical properties of glassy polymers at high strain rates and confinement were recently investigated: PMMA by Rittel and Brill (2008), and polycarbonate by Rittel and Dorogoy (2008). Rittel and Brill (2008) reported that under a suitable confinement level and high strain rate, PMMA can undergo a brittle–ductile transition resulting in the formation of an adiabatic shear band. Impact and perforation of PMMA plates have been investigated by Rosenberg et al. (2005) who showed an interesting ricochet phenomenon that occurs for inclined impacts. In their simulations the actual mechanical properties of PMMA were not used, but were systematically varied until a satisfactory similarity between the experiments and the simulations was obtained. Their main conclusion was that spalling (dynamic tensile failure) is the main responsible factor for the generation of the ricochet. Dorogoy et al. (2010, 2011) addressed the high speed impact (~1 (km/s)) and perforation of PMMA and polycarbonate plates by short armor piercing projectiles using the actual strain rate dependent properties and failure criteria for the combined effects of brittle spalling and ductile deformations. A comparison to a set of experiments validated the simulations.

In this *hybrid* experimental–numerical investigation the response of *thick* monolithic PMMA plates to impact of long steel projectiles is investigated. A gas gun is used to

* Corresponding author. Tel.: +972 77 887 3261.
E-mail address: merittel@technion.ac.il (D. Rittel).

0167-6636/$ - see front matter © 2013 Elsevier Ltd. All rights reserved.
http://dx.doi.org/10.1016/j.mechmat.2013.11.010

accelerate the projectiles to *low* impact velocities in the range of 100 (m/s) < V_0 < 250 (m/s). The response of such plates to the impact of *long* steel rods with either blunt, hemispherical or ogive-head projectile is determined. The tests are supplemented with explicit 3D numerical analyses using ABAQUS explicit (2012). The simulations use a Drucker–Prager (Bardia and Narasimhan, 2006) material model for the PMMA, which captures the *actual* strain rate and pressure sensitivity. Two failure criteria which correspond to the *combined* effects of brittle spalling/cracking and ductile deformations are used. A user subroutine of type VUSDFLD (Abaqus, 2012) is added to apply failure at a specified maximum principal stress.

The paper is organized in the following way: First the experimental set up is detailed followed by the experimental results. Next the numerical model is described in detail, followed by the simulations' results. A discussion comes next, followed by a summary and conclusions.

2. Experimental setup

Thick square PMMA plates were impacted by long hard steel projectiles. A square PMMA plate with width W = 124 (mm) and thickness t = 40 (mm) is shown schematically in Fig. 1(a). The steel projectiles have a diameter D = 6 (mm) and lengths of L = 56 (mm) and 72 (mm), as shown in Fig. 1(b). These dimensions correspond to the non-dimensional values L/D = 9.3 and 12 respectively, which are considered as "long" projectiles (typical AP projectiles has 3 < L/D < 5). The plate is considered "thick" since t/D = 6.67 ("thin" plates are when t/D < 1). Except for their lengths, the projectiles differed by the shape of their head. Three head geometries were used: blunt, hemispherical and ogive, as shown in Fig. 1(b) (I–III), respectively. The ogive head length was L_1 = 10 (mm) which corresponds to 3CRH (Caliber Radius Head), The 56 (mm) length projectile weighs 12.4 (gr), 12.1 (gr) and 11.4 (gr) respectively,

The projectiles are accelerated by a gas gun shown in Fig. 2(a). The gun consist of two main parts: A pressurized gas tank and a long tube (~2 m) having an inside diameter of 40 (mm). A velocity meter which consist of two photovoltaic cells is mounted close to the muzzle of the tube and measures the initial impact velocity. Hydraulic valves control the filling of the tank with pressurized air or helium and its release into the tube which accelerates the projectile. The process is controlled from the control table shown in Fig. 2(a). The projectile is fired towards the target which is enclosed in a thick aluminum box shown in Fig. 2(b). The gun muzzle, Fig. 2(c) is inserted into the inlet of the box. The thick box avoids unwanted projections of debris that might endanger the staff running the experiments. One side of the box is made from transparent polymer which allows for high speed camera recording of the impact.

The projectiles are stabilized in their flight by a polymeric sabot which gets destroyed upon impact. A section through the sabot with its dimensions is shown in Fig. 3(a). The sabot is made by Objet 3D printer from FullCure720, and it weighs 6.1 (gr). The printing technique greatly reduces (machining) production costs while ensuring a high degree of reproducibility. The assembly of a projectile into the sabot and the PMMA plate at the moment of impact are shown in Fig. 3(b).

The maximum achievable velocity at impact is V = o(300) (m/s), which is "slow" compared to the velocity of AP projectiles 0.75 (km/s) < v < 2 (km/s). Yet, such a velocity is highly representative of impact of various kinds of debris. A high speed camera (Cordin-530 – 200 kfps) was mounted perpendicular to the line of fire as shown on Fig. 2(b). A total of 16 pictures were taken at time interval of ~20 (μs) between each frame.

3. Experimental results

The evolution of penetration of two projectiles which differ *only* by their head geometry (hemispherical and ogive) is shown in Fig. 4. The measured impact velocity of the ogive projectile was 146 (m/s) and the measured

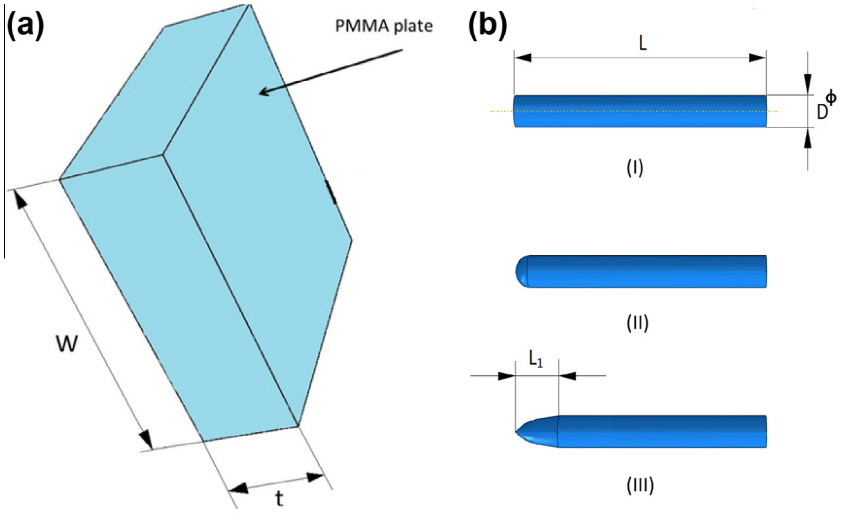

Fig. 1. (a) The impacted thick square PMMA plate. (b) The steel projectiles: (I) blunt, (II) hemispherical and (III) ogive.

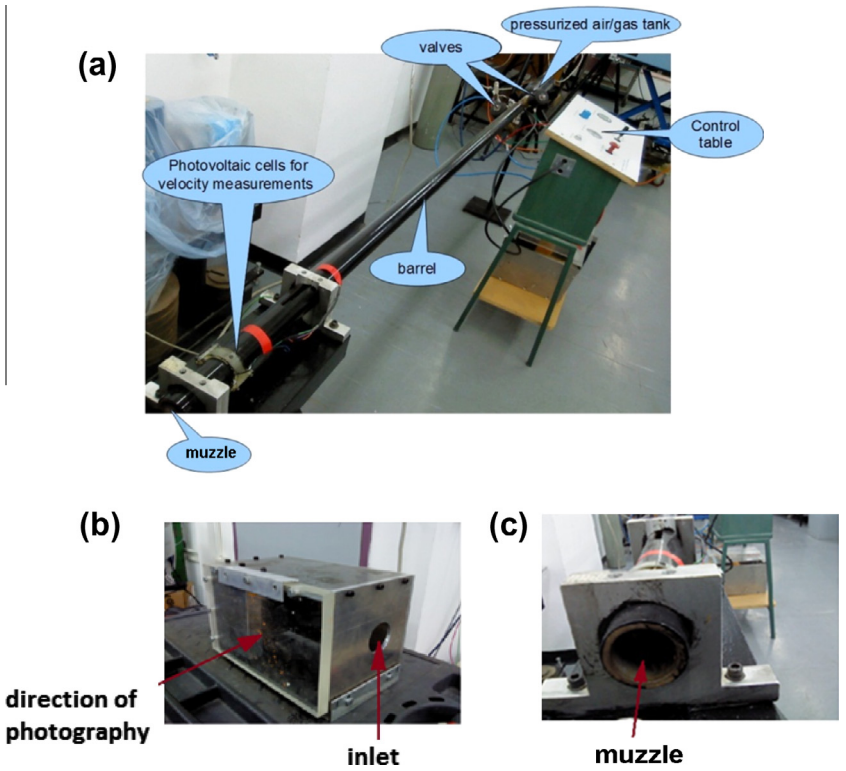

Fig. 2. (a) The air/helium gun. (b) The safety box in which the impact takes place. (c) The muzzle of the gun bore which is inserted into the safety box.

impact velocity of the hemispherical projectile was 142 (m/s). Fig. 4(a), (c), (e) and (g) correspond to the hemispherical-headed projectile, while Fig. 4(b), (d), (f) and (h) correspond to the ogive-headed projectile. The projectiles and the plate after $t \sim 23$ (μs) of impact are shown in Fig. 4(a) and (b). It can be observed that during this time interval, the damage is mostly ductile and surrounds the projectiles' heads. The projectiles and plate at time $t = 61$ (μs) are shown in Fig. 4(c) and (d). Note that at this time, radial cracks have developed and some material is flowing backwards probably due to spalling around the penetration hole. The cracks due to the impact of the ogive projectile are much more developed than those caused by the hemispherical projectile. It can also be observed that for the same time period, the ogive projectile penetrated deeper than the hemispherical one. Fig. 4(e) and (f) are showing the plate and projectiles at approximately the maximum depth of penetration. For the hemispherical projectile, this occurs after $t = 99$ (μs), while the penetration process of the ogive projectile lasts longer up to $t = 137$ (μs). The DoP (depth of penetration) of the ogive projectile is higher than that of the hemispherical projectile. For both projectiles the radial cracks grow in a brittle manner during the whole penetration process. Fig. 4(g) and (h) show that both projectiles *have bounced backwards* after reaching the maximum penetration depth. During this time the cracks continue to grow due to stress waves running in within the PMMA plate. It should be emphasized that the bounce back phenomenon occurs only when plate penetration is incomplete, as happens at the lower impact velocities.

The impact damage due to three 56 (mm)-long projectiles with blunt, hemispherical and ogive heads are shown in Fig. 5(a)–(c), respectively. The measured impact velocities were: 221, 221 (m/s) and 230 (m/s) respectively. The pictures shown here were taken at $t \sim 109$ (μs) , $t \sim 116$ (μs) and $t \sim 158$ (μs) after first contact with the impacted face of the plate, at a stage where the projectiles have reached their maximum DoP. Their corresponding estimated DoP's are: 8, 10, 19 (mm) respectively. The radial cracks which have developed from the projectiles' impact trajectory are clearly visible. Here too, these cracks continue to grow after the projectiles have reached their maximal DoP's. At that stage, the projectiles bounce once again backwards while the cracks continue to grow due to the stress waves which travel within the PMMA target plates. The growing damage due to the impact of the three receding projectiles at time $t = 247$ (μs) (blunt), $t = 271$ (μs) (hemispherical) and $t = 295$ (μs) (ogive) is shown in Fig. 5(d)–(f).

Damaged PMMA plates due to impact of 72 (mm) long projectiles launched at 220 m/s are shown in Fig. 6, for blunt (a) and hemispherical (b) heads. Two regions of damage can be observed: a narrow region close to the projectile trajectory in which the damage is mostly ductile, and a wider region of brittle damage where large hemispherical dish-like and radial cracks have grown.

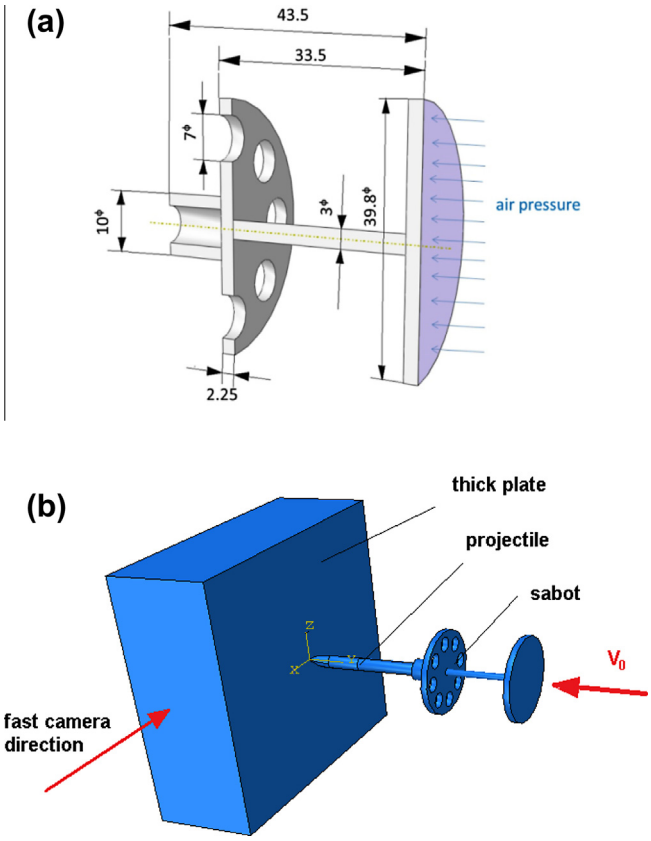

Fig. 3. (a) A section through the sabot showing its dimensions. (b) Experimental setup showing the PMMA plate and the projectile with its sabot at the moment of impact.

3.1. Summary of experimental results

The penetration can be divided into 3 stages:

1. Entrance.
2. Propagation.
3. Backwards bouncing.

The first step lasts for ~25 (μs) during which the head of the projectile penetrates the plate and the deformation is mostly ductile (Fig. 4(a) and (b)). A plastic region surrounds the heads, causing a later nucleation of cracks.

In the second step the projectile partly penetrates the plate and comes to a complete stop. This step is characterized with crack development and growth. The cracks start in the close vicinity of the penetration track and propagate both radially and hemi-spherically (dish-like cracks). Cracking seems to be a brittle process due to stress waves. Debris because of spalling and from the projectile crater are ejected backwards (impacted side).

In the third step, the projectile, which has reached its maximum DoP, bounces backwards while the cracks continue to grow due to stress waves within the target (Fig. 5(d)–(f)). Such a "strong" bouncing effect has not been reported for other materials to the best of the authors' knowledge.

4. Numerical simulations

The impact was simulated with Abaqus explicit 6.12-2 (2012) using a 3D model. One step of 400 (μs) was simulated. A user-subroutine in which failure is due to maximum principal stress was written and added to the numerical code. The details of the analysis are described in the sequel.

4.1. Geometrical model, mesh and boundary conditions

Because of the symmetry of the problem, only half of the physical domain was modeled as shown in Fig. 7. The 3D model contains 3 parts: sabot, projectile and a plate. The dimensions of the plate and projectile are shown in Fig. 1(a) while the dimensions of the sabot are shown in Fig. 2(a). The three parts are initially in contact.

The mesh of the sabot contained 24,264 linear tetrahedral elements of type C3D4 with 6021 nodes. The mesh of the ogive head projectile contained 1222 linear hexahedral elements of type C3D8R with 1745 nodes. The meshed plate contained 138,400 linear hexahedral elements of type C3D8R with 146,001 nodes. A typical size of the elements in the projectile and along the trajectory of the projectile was 1 (mm). The mesh is shown in Fig. 7.

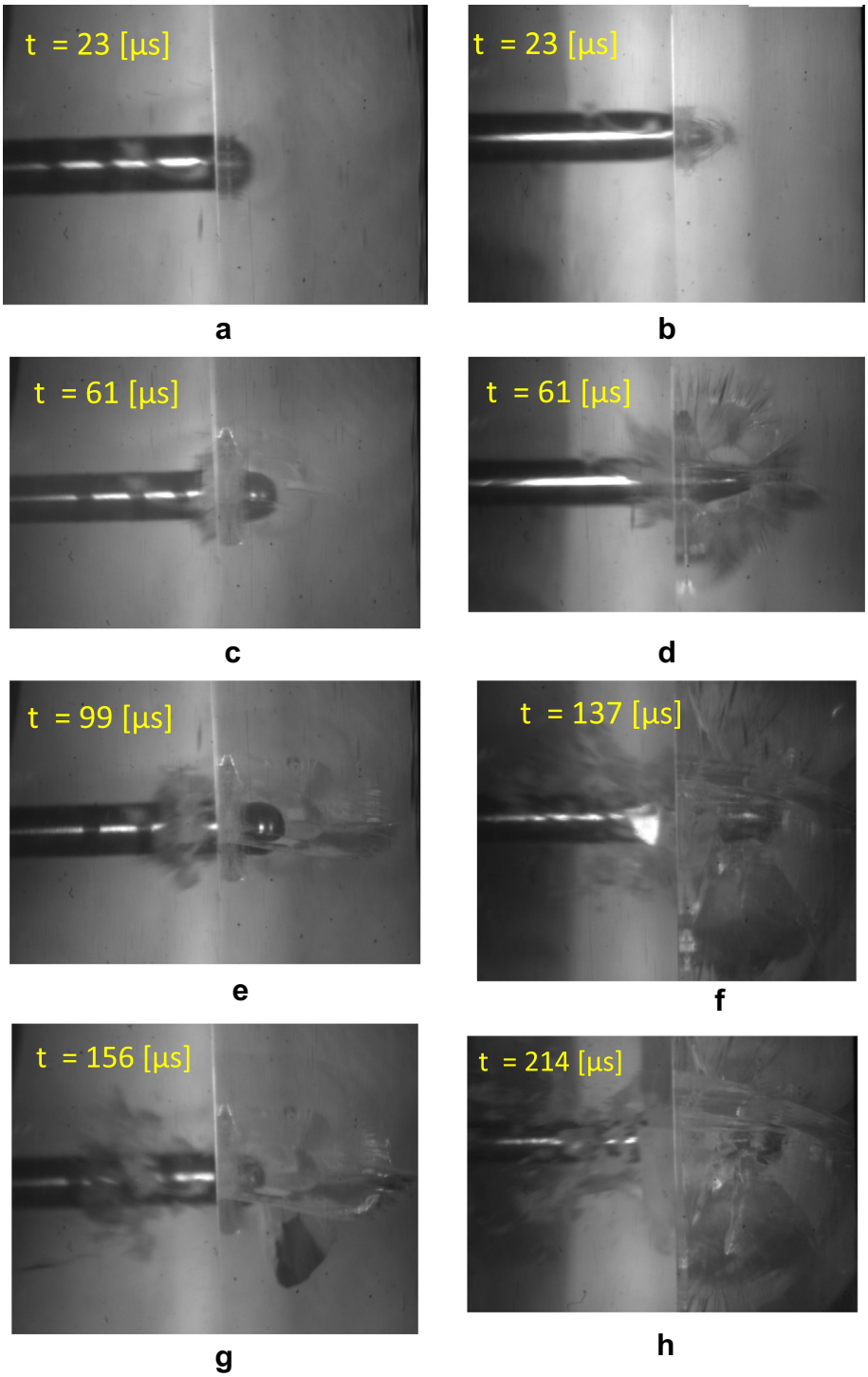

Fig. 4. Pictures of spherical and ogive head projectile which impacted at 142 (m/s) and 146 (m/s) respectively. (a) $t = 23$ (μs). (b) $t = 23$ (μs). (c) $t = 61$ (μs). (d) $t = 61$ (μs). (e) $t = 99$ (μs). (f) $t = 137$ (μs). (g) $t = 156$ (μs). (h) $t = 214$ (μs). The pictures show three stages in the penetration process: entrance, propagation and backward bouncing.

The assembled projectile was given initial velocity of 220 (m/s). Symmetry conditions were applied along the line of symmetry. The general contact algorithm of Abaqus (2012) was used with element-based surfaces which can adapt to the exposed surfaces of failed elements. Abaqus frictionless tangential behavior with the penalty formulation was adopted. All the surfaces of the plate that may become exposed during the analysis, and are originally in

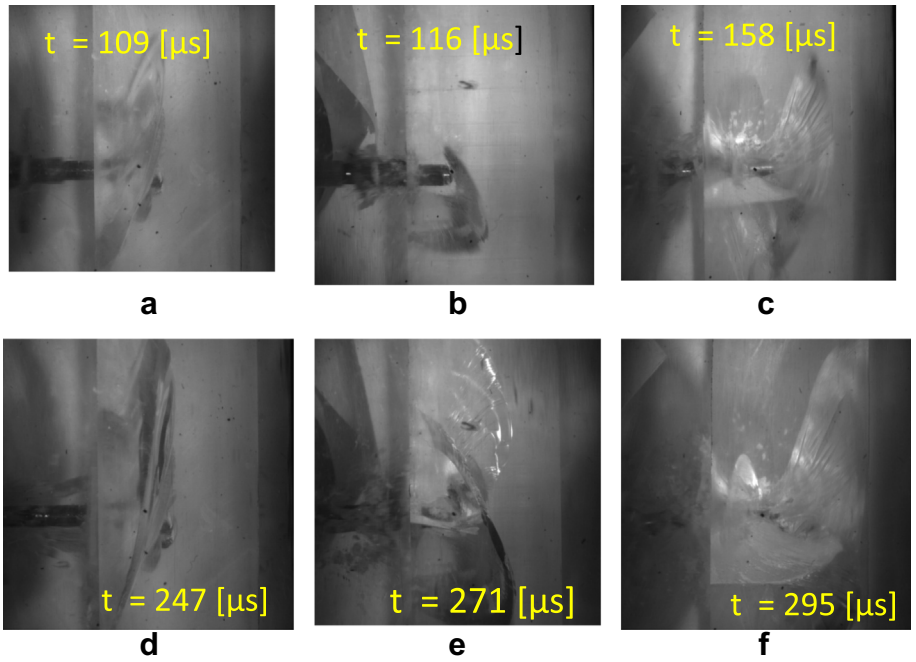

Fig. 5. Pictures of blunt hemispherical and ogive head projectile which impacted at 221, 221 and 230 (m/s) respectively. Figures (a)–(c) were taken at approximately at maximum DoP. (a) Blunt head projectile at $t = 109$ (μs). (b) Hemispherical head projectile at $t = 116$ (μs). (c) Ogive head projectile at $t = 158$ (μs). (d) Blunt head projectile at $t = 247$ (μs). (e) Spherical head projectile at $t = 271$ (μs). (f) Ogive head projectile at $t = 295$ (μs).

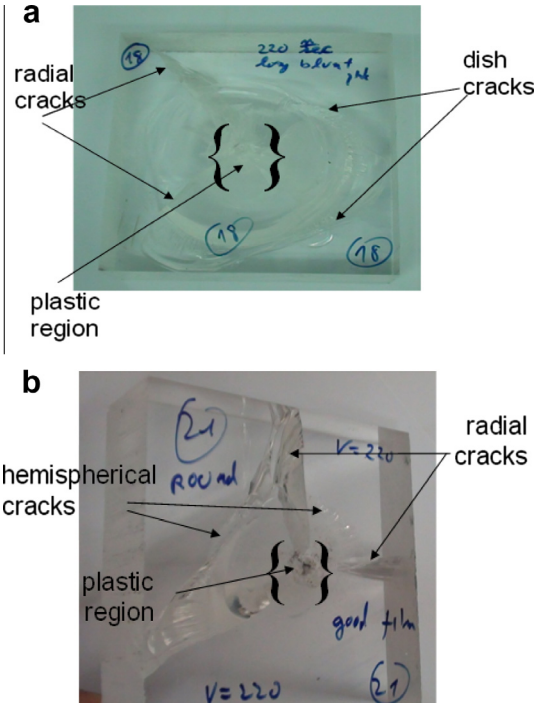

Fig. 6. Damaged PMMA plates due to impact of 72 (mm) long projectiles impact at $v = 220$ (m/s). (a) Blunt. (b) Hemispherical. Note the ductile damaged area adjacent to the trajectory and the large region of brittle damage where hemispherical and radial cracks have propagated.

the interior of plate, were included in the contact model. Therefore, all the elements of the plate were included in the contact domain since the projectile trajectory is not known a-priory. In the contact algorithm, the contact nodes still take part in the contact calculations, even after all of the surrounding elements have failed. These nodes act as free-floating point masses that can experience contact with the active contact faces.

4.2. Material models and failure parameters

4.2.1. Sabot

The sabot weighted 6.1 (gr) and was solid-printed from FullCure720, which is a rigid general purpose semi translucent acrylic-based photopolymer. An elastic plastic material model was used with Mises plasticity. For this material, the density used is $\rho = 1050$ (kg/m^3) and Young's modulus $E = 2.87$ (GPa) with Poisson's ratio $\nu = 0.35$. The yield stress is $\sigma_y = 60$ (MPa). A small linear hardening was assumed with $E_p = 5$ (MPa). The ductile failure criterion was used (Abaqus, 2012), with no damage evolution. The equivalent plastic failure strain was 0.2 for all strain rates and triaxialities.

4.2.2. Projectiles

The projectiles were made of hardened 15-5 PH stainless steel with density $\rho = 7800$ (kg/m^3). The corresponding mass of the 56 (mm) long projectiles with blunt, hemispherical and ogive heads were: 12.4 , 12.1 and 11.4 (gr), respectively. An elastic–plastic material model was used with Young modulus $E = 210$ (GPa) and Poisson's ratio $\nu = 0.3$. Mises plasticity was assumed with a yield stress $\sigma_y = 1.5$ (GPa), and (linear) hardening modulus of $E_p = 1.67$ (GPa). No failure criterion was used since the hard

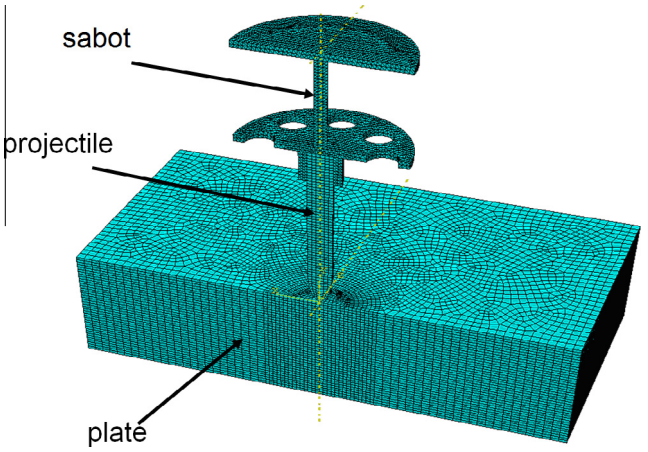

Fig. 7. The numerical 3D model with a typical mesh. The model includes three parts: sabot, projectile and a plate.

steel projectile did not fail or got damaged in those experiments.

4.2.3. PMMA plate

The plate was made of polymethylmethacrylate (PMMA) with density $\rho = 1190$ (kg/m^3) and weighted 0.732 (kg). Here too, an elastic–plastic material model was used with Drucker–Prager plasticity (Bardia and Narasimhan, 2006; Rittel and Dorogoy, 2008) with a frictional angle of $\beta = 20°$. The elastic properties which were used: $E = 5.7$ (GPa) and $\nu = 0.42$ (Rittel and Maigre, 1996). Fig. 8 shows the strain rate dependent hardening which was also used in Dorogoy et al. (2010). Note that the flow stress increases with the strain rate. The value of the dynamic yield stress may almost reach four times the quasi-static value.

Two failure criteria were used *simultaneously* : (1) Ductile failure with damage evolution (Dorogoy et al., 2010, 2011). (2) Maximum principal stress. An element was deleted from the analysis when one of these two criteria was first fulfilled.

Criterion (1) is fully detailed in Abaqus (2012) and was also used in (Dorogoy et al., 2010, 2011). The plastic failure strains for different strain rates and triaxiality (t_r) are detailed in Fig. 9. It can be observed the failure strain decreases with the strain rate for all triaxiality levels. The failure strains for positive triaxiality are the same as those used in Dorogoy et al. (2010). The failure strains for negative triaxiality were determined by fitting the numerical results to the observed experimental results. It can be observed that the higher the (absolute value) negative triaxiality, the higher the failure strain.

Damage evolution was modeled by an equivalent plastic displacement at the point of failure: $u_p^f = 120$ (μm). Those values were calibrated by fitting the velocities of the projectiles and their depths of penetration to the experimental results (including those which appear in Part II). In the second criterion "maximum principal stress", an element was deleted from the analysis (i.e. zero values were applied to the stresses within the elements) once the maximum principal stress within the element reached a predefined critical value: $\sigma_1^{\max} = 400$ (MPa). This value is three times the "tensile failure" value 133 (MPa) which was used in Dorogoy et al. (2010). Since Abaqus does not include this failure criterion, the latter was applied by means of a user subroutine of the VUSDFLD type.

5. Numerical results

The results shown here are due to impact at 220 (m/s) of three types of steel projectiles having the same

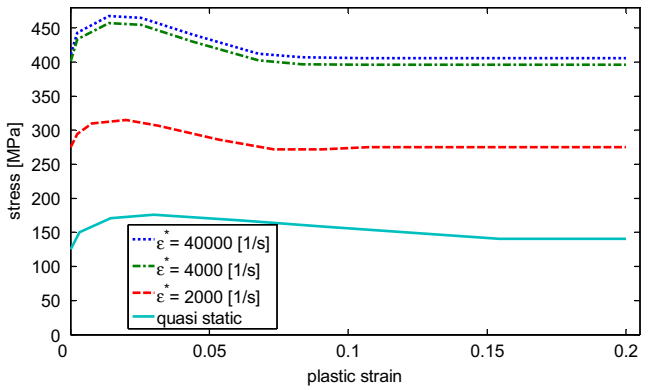

Fig. 8. Stress – plastic strain curves of PMMA for various strain rates.

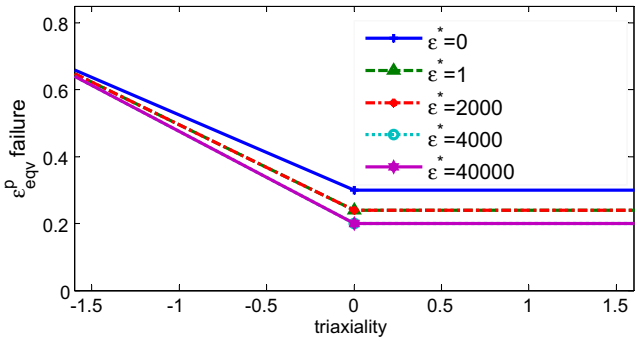

Fig. 9. Plastic failure strains of PMMA for various strain rates and triaxialities.

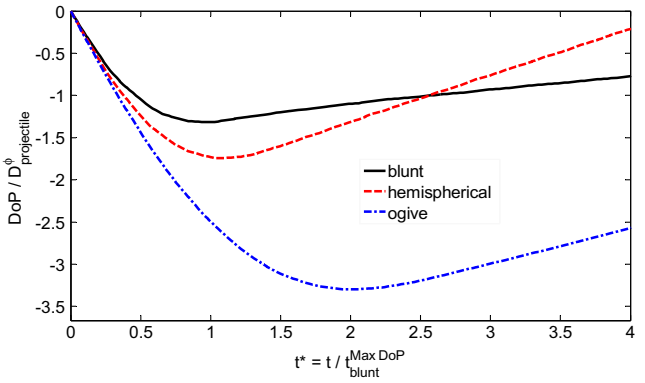

Fig. 10. Vertical displacements of blunt, hemispherical and ogive nose projectile which impact at 220 (m/s) a PMMA plate of 40 (mm) width.

diameter, $D = 6$ (mm), and length , $L = 56$ (mm), but with different head geometries (Fig. 1(b)). The normalized vertical displacements of the tips of the heads of the projectiles vs. normalized time are plotted in Fig. 10. Displacements are normalized by the diameter of the projectile. Time is normalized by the time needed for the blunt head projectile to reach its maximum depth of penetration (DoP). The tips are the center point on the surface of the head. The DoPs obtained from these curve are: 7.9, 10.1 and 19.8 (mm) respectively and they are reached at time: 83 , 92 and 171 (μs). At greater times, the displacement changes direction and the projectiles move backwards as observed in the experimental results. This phenomena was obtained numerically also by Rosenberg and Dekel (2009), who used short ogive nosed AP projectiles on aluminum at high velocities 0.5–1.5 (km/s), calling it "spring-back effect".

The measured DoP's of these tests, shown in Fig. 5(a)–(c), are 8, 10 and 19 (mm) respectively. The numerical results *correspond quite well* to the experimental ones. One should note here that the measurement of the experimental DoP is not highly accurate for technical reasons (nature of the crater with jagged edges), so that at this stage, the agreement between the numerical predictions and the experimental DoP values can be considered as satisfactory.

From the calculations and the experiments, it appears, as expected, that the ogive-shaped projectile is the potentially most dangerous of the three tested projectiles. The second part of this paper will elaborate further on this specific geometry.

The "bounce back effect" seems to be very significant in PMMA, hence we further investigated it. We concluded that the phenomenon occurs due to concentration of *elastic strain energy* just below the penetrating projectile head. Fig. 11(b)–(d) show the variation of the elastic strain energy density (ESEDEN) at a time close to that at which the projectiles have reached their maximum DoP's. It shows that underneath the projectile's head, in a region approximately twice the projectile diameter, one finds a strong concentration of elastic energy that can be transformed back into kinetic energy of the projectiles. This energy is released by applying pressure on the projectile heads and pushing them to the opposite direction, thus transforming the locally stored elastic energy into kinetic energy of the projectile.

The evolution of the total internal energy (IE) of the PMMA plate and the total kinetic energy (KE) of the projectile during the impact of the *hemispherical* projectile are plotted in Fig. 12. The time at which the KE reaches a minimum corresponds to the time of maximum DoP of the projectile (calculated to be $t = 91.1$ (μs)). The normalized time in Fig. 12 is therefore normalized by this value ($t^* = t / t^{Max\ DoP}$) while the energies are normalized by the value of the kinetic energy of the projectile prior to impact. The time of minimum KE correspond to the time of maximum IE. After that time the KE increases slightly while the

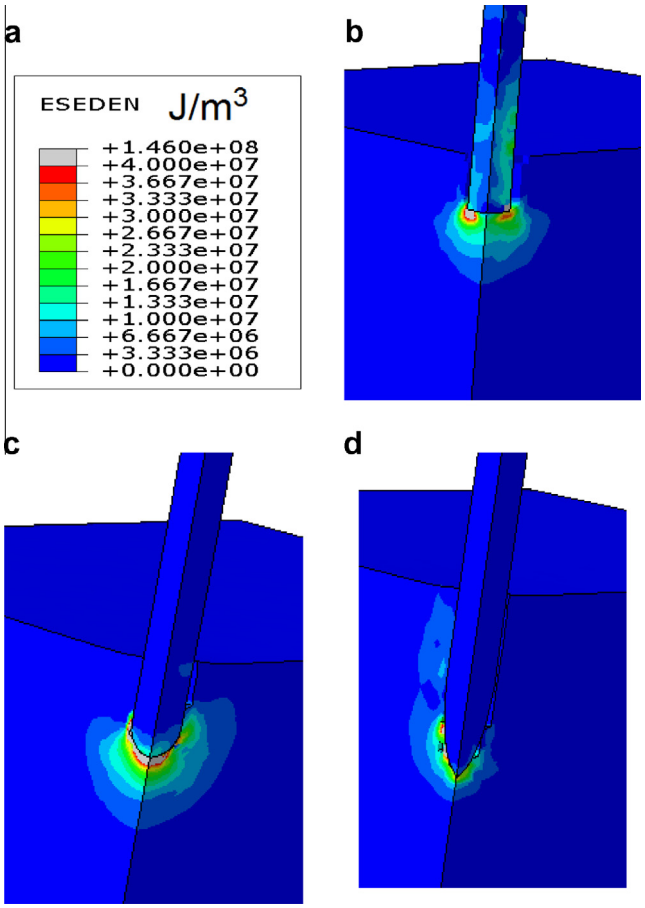

Fig. 11. The distribution of elastic strain energy density underneath the projectiles heads at time close to their maximum DoP's . (a) A color map of ESEDEN. (b) Blunt head projectile. (c) Hemispherical head projectile. (d) Ogive head projectile.

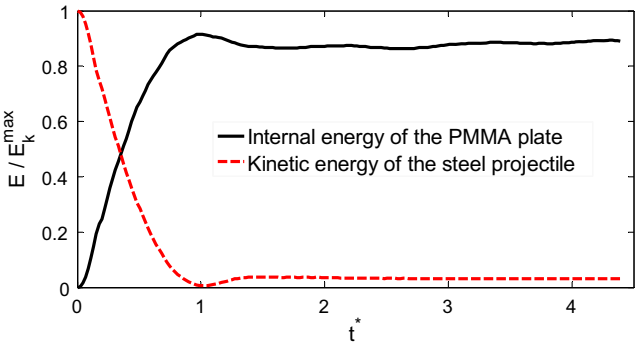

Fig. 12. The total kinetic energy of the hemispherical head projectile in comparison to the total internal energy of the plate.

IE decreases only very slightly. The drop in the IE is due to transformation of elastic strain energy (which is part of the total internal energy of the plate) to kinetic energy of the projectile moving in the opposite direction. About 4% of the IE is converted to kinetic energy of the projectile.

The projectiles in the numerical analyses were not treated as rigid but as elastic, therefore capable of experiencing stress waves during the penetration process. Consequently, quantities such as displacements, velocities and accelerations differ slightly at each position in the projectile and do oscillate with time. The oscillations are also due to the waves in the PMMA plate as well as the discontinuous nature of the element removals underneath the tip. Fig. 13 shows the variation with normalized time of the normalized velocity of the tip of the *ogive* projectile. The time is normalized by the time of maximum DoP: 172 (μs). The

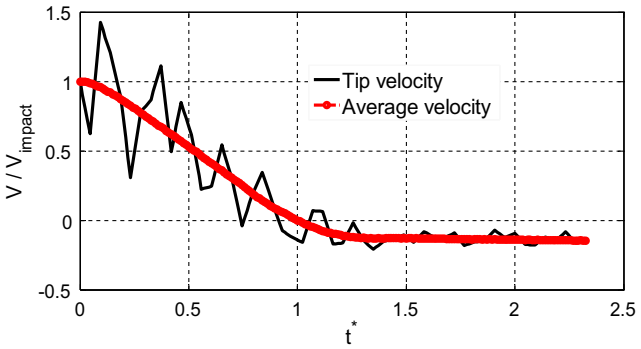

Fig. 13. Evolution of the tip of the ogive head's velocity, along with the averaged velocity of the whole projectile.

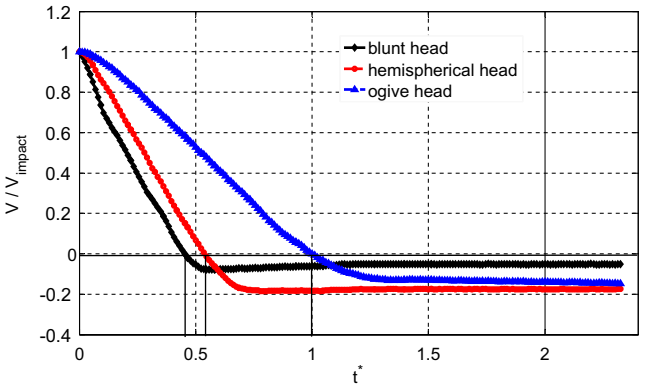

Fig. 14. Normalized averaged velocities of the blunt hemispherical and ogive-head projectiles.

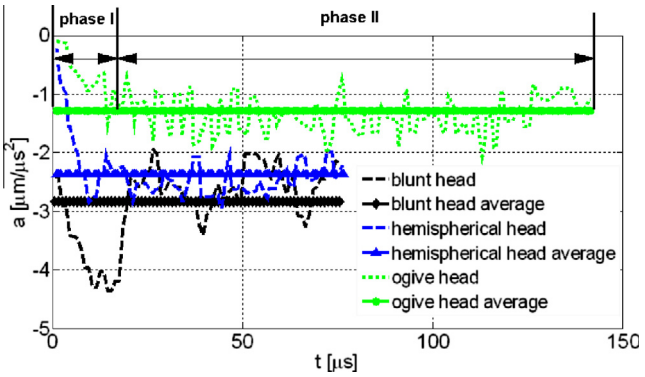

Fig. 15. The averaged instantaneous decelerations together with their constant approximations.

velocity is normalized by the impact velocity: 220 (m/s). It also shows an average of the velocities of all the elements within the projectile (1222 elements) which are approximately the same size. It can be observed that the average value which represents the behavior of the whole projectile agrees very well with the velocity of the tip of the projectile. The average values of the whole projectile do not oscillate as the values of local tip point. The velocity becomes negative for normalized time greater than 1 because the projectile bounces backwards.

The "bounce-back effect" is shown in Fig. 14 for all three head geometries. During most of the penetration time the slope of the curve is quite constant, indicating that the average deceleration of each projectile may be approximated by a constant value. This suggests that a simple formula may be adopted to connect the impact velocity (V_0), DoP and deceleration (a): $a = V_0^2/(2 * \mathrm{DoP})$. Linear approximation yields: 2.79, 2.50 and 1.38 (μm/μs^2) for the blunt, spherical and ogive-nosed projectiles respectively. Note that the deceleration of the blunt projec-

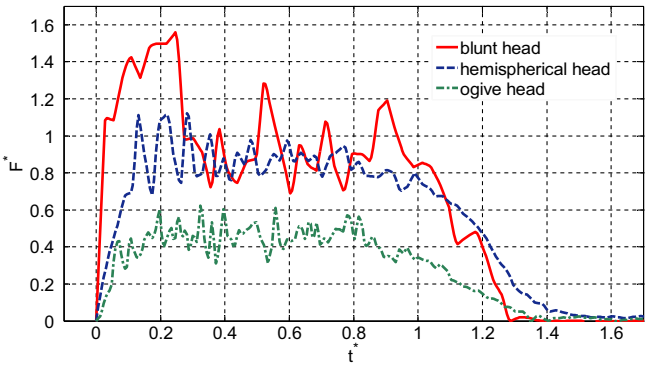

Fig. 16. The instantaneous resisting force that the PMMA target exerts on the penetrating projectiles.

tile is higher than that of the hemispherical and ogive-head projectiles. This means that the resisting force to penetration is higher. The slope of the ogive-head projectile is the lowest which means that the target exerts a lower resisting force to penetration, yielding a deeper penetration. All three curves show that the averaged deceleration drops (the slope becomes zero) when the projectile bounces backwards.

For further investigation of the instantaneous averaged deceleration behavior, the values of Fig. 14 were differentiated with respect to time using finite differences with accuracy $O(\Delta t^2)$ and $\Delta t = 1$ (μs). The results are shown in Fig. 15 together with the linear approximation which yields a constant value.

Observing the instantaneous averaged deceleration of the hemispherical and ogive-head projectiles, it can be seen that the deceleration has two phases First, the entrance phase, where it increases in a relatively short duration until it reaches its average value. After entrance, the deceleration remains approximately constant until the projectiles reach their maximum DoPs. Thereafter, deceleration decreases to zero. The first two phases of the ogive projectile are marked in Fig. 15. The deceleration results for the blunt-head projectile are more wavy and it is hard to estimate the entrance phase duration but the values converge to the average value. The sharper the shape of the head, the longer the entrance phase. The entrance duration is ∼7 (μs) for the hemispherical head and ∼ 15 (μs) for the ogive head. Since the penetration process until maximum DoP lasts for 76 (μs), 91 (μs) and 172 (μs) for blunt hemispherical and ogive-head projectiles respectively. These result indicates that the entrance phase lasts on the average for ∼8% of the penetration time.

The instantaneous resisting force that the PMMA target exerts on the penetrating projectiles was calculated by Abaqus by integrating all the contact forces over the outer skin of the projectiles. The results are shown in Fig. 16. The forces are normalized by the average resisting force of the blunt head projectile calculated by $F = M * a_{\text{average}} = 34.48$ (kN). The time for each projectile is normalized by its maximum DoP time. Note the resemblance between Figs. 16 and 15 which were obtained by two different methods. The resisting force of the blunt head projectile is slightly higher (∼10%) than that of the hemispherical-head projectile, and much higher (∼200%) than that of ogive-head projectiles. A low deceleration corresponds to lower resisting force and higher DoP. Three regions can be observed: (1) $0 \leqslant t^* \leqslant 0.1 - 0.2$ increasing deceleration. (2) $0.1 - 0.2 \leqslant t^* \leqslant 1$ constant deceleration. (3) $1 \leqslant t^* \leqslant 1.5$ decreasing deceleration. It can be observed that for $t^* > 1$ the force gradually drops to zero. This confirms again that the ogive projectile penetrates the target with the greatest ease.

6. Discussion

A hybrid experimental–numerical characterization of the behavior of thick PMMA plates ($t/D = 6.67$) subjected to low velocity impact 100 (m/s) < V_0 < 250 (m/s) of long steel projectiles ($L/D = 9.3$) has been conducted. The numerical analyses complemented the observed experimental results and added insight regarding the variation of the field variables such as: stresses, strains, displacements, energies and forces. Although a good agreement was obtained regarding the trajectory of the projectiles which is mostly due to ductile failure, the numerical analyses fail to simulate the brittle damage due to crack propagation which stem out of the ductile region around the trajectory.

In most of the reported experiments (especially with blunt and hemispherical heads), complete perforation of the plate was not achieved, even if in some cases, radially propagating cracks would cause its rupture. For such incomplete penetration cases, an interesting phenomenon was observed, namely that the projectile always bounces backwards instead of arresting in the plate being stuck there. The numerical analyses showed that underneath the projectile's head, there is an accumulation of strain energy which transforms back into kinetic energy, imparted to the arrested projectile which thus bounces backwards.

In addition, this study showed that two main failure mechanisms operate simultaneously. The first which is the penetration mechanism itself, is of a ductile nature, as was reported for PMMA under large levels of confinement and sufficiently significant strain rates (Satapathy and Bless, 2000; Rittel and Brill, 2008). This process is energy consuming and controls the projectile's maximum DoP. The second failure mechanism which consists of

radial and dish-like crack propagation is the destructive one. Such brittle failure mechanism was not reported for polycarbonate (Dorogoy et al., 2011).

Those observations suggest that if one can devise a simple way to minimize or suppress the brittle failure mechanism, damage will only consist of its ductile component which is more energy consuming. A viable solution to delay or significantly reduce brittle cracking consists of applying a sufficient confinement which not only acts as a crack retarder but also confers additional strength to the polymer because of its relatively high pressure sensitivity.

Consequently, the natural extension of the present work deals with the effects of hydrostatic confinement on the overall ballistic performance of identical PMMA plates, which are subjected to the same impact tests, as reported in part II of this paper.

7. Conclusions

- Incomplete normal impact of PMMA plates in the low velocity regime by long rod type projectiles reveals a bounce back phenomenon.
- Numerical modeling of the experiments reveals that the bounce back phenomenon results from the conversion of stored elastic strain energy into kinetic energy imparted to the projectile which causes its ejection.
- As expected, of the three geometries that were investigated, the ogive headed projectile is the most deleterious as confirmed by the numerical analyses.
- Damage imparted to the plates is twofold, as it consists of a ductile penetration failure along with the later development of radial and hemispherical brittle cracks that can eventually lead to total fracture of the plate.
- It is therefore obvious that the latter mechanism should be significantly reduced in order to confer a superior penetration resistance to this glassy material.
- In order to minimize the brittle cracking effects, hydrostatic pressure can be applied to the plate. Application of such a pressure is reported in the second part of this paper.

Acknowledgments

The support of PMRI Grant # 2015267 is gratefully acknowledged. Dr. A. Belenky and Mr. Y. Rotbaum's and Mr. Z. Shachar's assistance with the high speed camera and production of the sabots is greatly appreciated.

References

Abaqus, 2012. Finite Element Package (explicit), v6, 12–2, 6.7.1 ed. Dassault Systemes Simulia Corp., Providence, RI.

Bardia, P., Narasimhan, R., 2006. Characterisation of pressure-sensitive yielding in polymers. Strain 42, 187–196.

Dorogoy, A., Rittel, D., Brill, A., 2010. A study of inclined impact in polymethylmethacrylate plates. Int. J. Impact Eng. 37, 285–294.

Dorogoy, A., Rittel, D., Brill, A., 2011. Experimentation and modelingof inclined ballistic impact in thick polycarbonate plates. Int. J. Impact Eng. 38, 804–814.

Rittel, D., Brill, A., 2008. Dynamic flow and failure of confined polymethylmethacrylate. J. Mech. Phys. Solids 56, 1401–1416.

Rittel, D., Dorogoy, A., 2008. A methodology to assess the rate and pressure sensitivity of polymers over a wide range of strain rates. J. Mech. Phys. Solids 56, 3191–3205.

Rittel, D., Maigre, H., 1996. An investigation of dynamic crack initiation in PMMA. Mech. Mater. 23, 229–239.

Rosenberg, Z., Dekel, E., 2009. On the deep penetration and plate perforation by rigid projectiles. Int. J. Solids Struct. 46, 4169–4180.

Rosenberg, Z., Surujon, Z., Yeshurun, Y., Ashuach, Y., Dekel, E., 2005. Ricochet of 0.3 " AP projectile from inclined polymeric plates. Int. J. Impact Eng. 31, 221–233.

Satapathy, S., Bless, S., 2000. Deep punching PMMA. Exp. Mech 40, 31–37.